Model Predictive Current Control of Grid-Connected Neutral-Point Clamped Converters to Meet Low Voltage Ride-Through Requirements

Alejandro Calle-Prado, *Student Member, IEEE*, Salvador Alepuz, *Senior Member, IEEE*, Josep Bordonau, *Member, IEEE*, Joan Nicolas-Apruzzese, *Student Member, IEEE*, Patricio Cortés, *Member, IEEE*, and Jose Rodriguez, *Fellow, IEEE*

***Abstract*— The low voltage ride-through requirement demands the wind power plants to remain connected to the grid in presence of grid voltage dips, helping actively the network overall control to keep network voltage and frequency stable. Wind power technology points to increase power ratings. Hence, multilevel converters, as for example, neutral-point clamped converters, are well suited for this application. Predictive current control presents similar dynamic response and reference tracking than other well-established control methods, but working at lower switching frequencies. In this work, the predictive current control is applied to the grid-side neutral-point clamped converter as part of a wind energy conversion system, in order to fulfill the low voltage ride-through requirements. Dc-link neutral-point balance is also achieved by means of the predictive control algorithm, which considers the redundant switching states of the neutral-point clamped converter. Simulation and experimental results confirm the validity of the proposed control approach.**

***Index Terms*— Low-voltage ride-through (LVRT), reactive support, voltage unbalance, predictive control, wind turbine.**

I. Introduction

THE installed power capacity and penetration of wind power generation has been growing significantly over the last decade [1]. Due to its increasing penetration, distributed generation has been included into the grid overall control system, to ensure the reliability and efficiency of the power system. The Grid Connection Requirements (GCRs) for conventional and distributed generation [2] are set by the power system operators. The current GCRs [3], [4] require the wind generators to remain connected to the grid during disturbances, as for conventional generators, condition known as the low voltage ride-through (LVRT) requirement.

The Wind Energy Conversion Systems (WECSs) with variable-speed wind turbines are mostly implemented with Doubly-Fed Induction Generators (DFIGs) [5], [6], because the power rating of the converter is about 30% of the machine nominal power. However, in comparison with DFIG, variable-speed WECSs based on a Permanent-Magnet Synchronous Generator (PMSG) with a full power converter [5], [7] do not require gearbox and provide extended speed operating range and full decoupling between the generator and the grid, which results in higher power capture at different wind speeds and enhanced capability to fulfill the LVRT requirement. These properties make this configuration interesting, even though converter losses increase.

Low-voltage two-level Voltage-Source Converters (VSCs) are the most used topology in WECS [8]. However, current-source converters [9] and multilevel topologies [10], [11] can be better suited than conventional VSCs for higher power levels, considering that WECSs currently tend to increase their power rating [1], [5].

Model Predictive Control (MPC) [12], [13] is a set of predictive control techniques based on the dynamic model of the process to be controlled and a time horizon. Among the different MPCs applied to power converters [13], [14], Finite Control Set MPC (FCS-MPC) [15]–[21] is particularly attractive as it takes advantage of the limited switching states of the converter for solving the optimization problem from a discrete model of the system. The switching action that minimizes a given quality function is directly applied to the power converter. Thus, no modulator is needed.

The inclusion of nonlinearities and constraints of the system is another advantage of the FCS-MPC, as they can be included in the control law straightforward [15], [22]–[24]. However, the accuracy of the FCS-MPC is affected by the precision at estimating the values for the system parameters [15].

Manuscript received November 21, 2013; revised March 4, 2014, May 9, 2014, and July 4, 2014; accepted July 25, 2014.

This work has been supported by the Ministerio de Ciencia e Innovación, Spain, under Grants CSD2009-00046.

A. Calle-Prado, J. Bordonau, and J. Nicolas-Apruzzese are with the Department of Electronic Engineering, Technical University of Catalonia, 08028 Barcelona, Spain (email: alejandro.calle@upc.edu; josep.bordonau@upc.edu; joan.nicolas@upc.edu).

S. Alepuz is with the Mataro School of Technology (Tecnocampus Mataró-Maresme), Technical University of Catalonia, 08302 Mataro (Barcelona), Spain (email: dr.salvador.alepuz@ieee.org).

P. Cortes is with is with the Power Electronic Systems Laboratory, ETH Zurich, Switzerland (email: cortes@lem.ee.ethz.ch).

J. Rodriguez is with the Department of Electronics Engineering, Universidad Técnica Federico Santa María, Valparaiso 2390123 Chile (email: jrp@usm.cl).

A number of control approaches, most of them based on conventional control theory and symmetrical components, are found in the literature for grid-connected VSCs [25]–[27] and for Neutral-Point Clamped converters (NPCs) [28], [29], under unbalanced grid condition. The use of predictive control techniques under an unbalanced grid found in the literature are mostly focused on the current control of two-level inverters [30], direct power control of two-level rectifiers [31], and DFIG [32]. However, predictive control applied to the NPC inverter to meet the LVRT requirement is hardly covered by the current literature in the field [16], [33].

This work is focused on the FCS-MPC of the grid-side NPC converter, in order to fulfill the LVRT requirements, as part of a WECS based on a PMSG and a back-to-back NPC full power converter, shown in Fig. 1. To do that, the dc-link voltage is assumed constant, as detailed in Section II, and the dc-link brake chopper, the generator-side converter, and their respective controllers are not included in the system model [34]. Results for the complete system shown in Fig. 1 with conventional control are found in [29]. The predictive control for the complete system is currently under development.

The proposed predictive control applied to the grid-side NPC converter provides balanced grid currents under grid voltage dip, concurrently with proper active and reactive power regulation, allowing to fully meet the LVRT requirement. Dc-link neutral-point voltage balance is also achieved by means of the predictive control algorithm, which considers the redundant switching states of the NPC.

Unlike controllers based on symmetrical components, the proposed predictive current controller does not need any Sequence Separation Method (SSM) for control purposes, therefore eventual inaccuracies after grid fault appearance and clearance, caused by the SSM, will disappear [16], [33].

Notice that some preliminary results have been published by the authors in [33], but the previous paper does not include accurate current reference calculation, experimental results, harmonic performance, and comparison of the number of commutations/losses with a conventional modulation strategy.

The paper is organized as follows: Section II presents the system and its model. Section III describes the predictive control. Simulation results are found in Section IV. Section V shows the experimental results obtained with the proposed control scheme. Finally, the conclusions are formulated in Section VI.

II. Model of the System

The system under study is shown in Fig. 2, along with the block diagram for the control, and the analysis is focused on the NPC grid-side converter and its controller.

The dc-link voltage is assumed constant [25], [34], [35]. In steady-state, the dc-link voltage is kept constant by the dc-link voltage regulator as shown, for instance, in [26], [28], [29]. Under dip condition, although the dc-link voltage can suffer some variation, it can be kept close to the nominal voltage by using a proper controller and/or hardware, as for instance, a dc-link chopper [28], [36], the energy storage in the rotor inertia [28], [29], or an undervoltage protection [28].

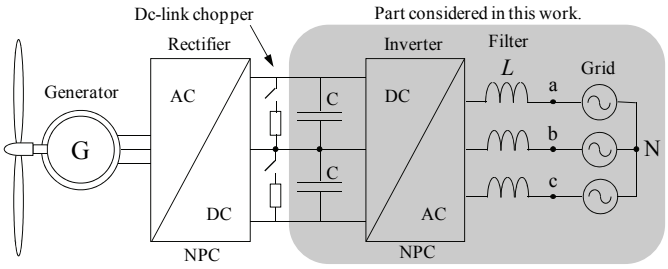

Fig. 1. Wind generator connected to the grid through a full power NPC back-to-back converter.

Therefore, this assumption can be considered realistic and proper and hence grid- and generator-side operations can be considered fully decoupled.

The grid-side model for the system in Fig. 2, to predict the grid current is obtained from

$$L\frac{di}{dt} = \left(v_{NPC} - e\right) - R \cdot i \tag{1}$$

where,

L	filter inductance
R	filter resistance
i	grid current vector
v_{NPC}	NPC voltage vector
e	grid voltage vector

The current and voltage vectors are defined by

$$i = \frac{2}{3}\left(i_a + a \cdot i_b + a^2 \cdot i_c\right) \tag{2}$$

$$v_{NPC} = \frac{2}{3}\left(v_{ao} + a \cdot v_{bo} + a^2 \cdot v_{co}\right) \tag{3}$$

$$e = \frac{2}{3}\left(e_a + a \cdot e_b + a^2 \cdot e_c\right) \tag{4}$$

where,

i_a , i_b , i_c	grid line currents
v_{ao} , v_{bo} , v_{co}	voltages generated by the NPC inverter
e_a , e_b , e_c	grid phase voltages

and $a = e^{j2\pi/3}$.

Considering a constant dc-link voltage, and balanced capacitor voltages, the voltages generated by the NPC at the inverter terminals are obtained from

$$v_{xo} = S_x \frac{V_{pn}}{2} \quad \text{where} \quad x = \{a, b, c\} \tag{5}$$

where the switching function S_x is defined according to the switching signals for the switches of each leg, as shown in (6).

$$S_x = \begin{cases} 1 & S_{x4} = on\ ,\ S_{x3} = on\ ,\ S_{x2} = off\ ,\ S_{x1} = off \\ 0 & S_{x4} = off\ ,\ S_{x3} = on\ ,\ S_{x2} = on\ ,\ S_{x1} = off \\ -1 & S_{x4} = off\ ,\ S_{x3} = off\ ,\ S_{x2} = on\ ,\ S_{x1} = on \end{cases} \tag{6}$$

The grid voltages and the line currents are obtained through their corresponding sensors, while the voltage vector generated by the NPC inverter is appropriately selected among the different 19 voltage vectors that can be obtained from the 27 switching states of the NPC inverter, shown in Fig. 3.

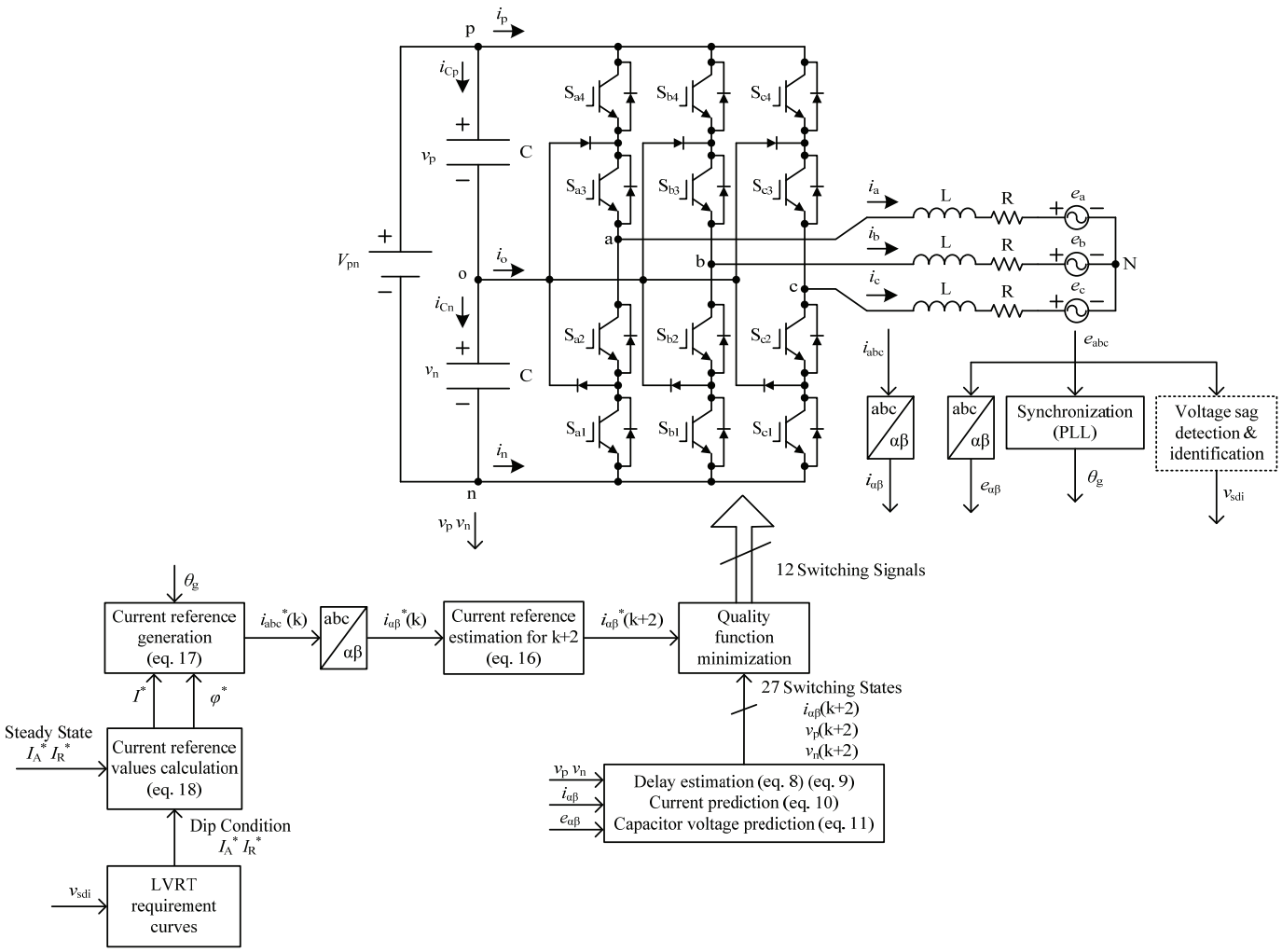

Fig. 2. Grid connected NPC inverter and control block diagram.

Applying a sampling period T_s, the derivative form (1) can be approximated as

$$\frac{di(t)}{dt} \approx \frac{i(k+1)-i(k)}{T_s} \tag{7}$$

Replacing (7) in (1), the relation between discrete-time variables is

$$i(k+1) = \frac{T_s}{L}\left[v_{NPC}(k) - e(k)\right] + \left(1 - \frac{R \cdot T_s}{L}\right) i(k) \tag{8}$$

The expression (8) is used to obtain predictions for the future value of the line current vector *i(k+1)*, considering all possible voltage vectors $v_{NPC}(k)$ generated by the inverter, the measured line current vector *i(k)* and grid voltage vector *e(k)*.

Following the same method as for the line currents, the discrete-time model for the dc-link capacitor voltages can be found, considering constant the dc-link voltage $V_{pn}=v_p(k)+v_n(k)$,

$$\begin{aligned} v_p(k+1) &= v_p(k) + \frac{T_s}{C} i_{Cp}(k) = v_p(k) + \frac{T_s}{2 \cdot C} i_o(k) \\ v_n(k+1) &= v_n(k) + \frac{T_s}{C} i_{Cn}(k) = v_n(k) - \frac{T_s}{2 \cdot C} i_o(k) \end{aligned} \tag{9}$$

where

v_p , v_n	dc-link capacitor voltages
i_{Cp} , i_{Cn}	currents through each dc-link capacitor
C	dc-link capacitor value
i_o	current through the dc-link midpoint.

The current through the dc-link midpoint i_o is obtained in (10) from the present *abc* currents i_a , i_b , i_c and the midpoint switching function S_{xo}. Here, S_{xo}, is a switching function corresponding to the dc-link midpoint, '*o*', obtained from the converter switching function, S_x, in (6), as detailed in (11).

$$i_o(k) = S_{ao}(k) \cdot i_a(k) + S_{bo}(k) \cdot i_b(k) + S_{co}(k) \cdot i_c(k) \tag{10}$$

$$S_{xo} = 1 \text{ if } S_x = 0, \text{ otherwise } S_{xo} = 0 \;\; ; \;\; x = \{a,b,c\} \tag{11}$$

Therefore, the future values of the dc-link capacitor voltages $v_p(k+1)$, $v_n(k+1)$ are obtained from (9)–(11), based on the present measured values of the dc-link capacitor voltages $v_p(k)$, $v_n(k)$, grid line currents $i_a(k)$, $i_b(k)$, $i_c(k)$, and the present applied midpoint switching function $S_{ao}(k)$, $S_{bo}(k)$, $S_{co}(k)$, so there is no need to measure the present value of the dc capacitor currents, $i_{Cp}(k)$ and $i_{Cn}(k)$.

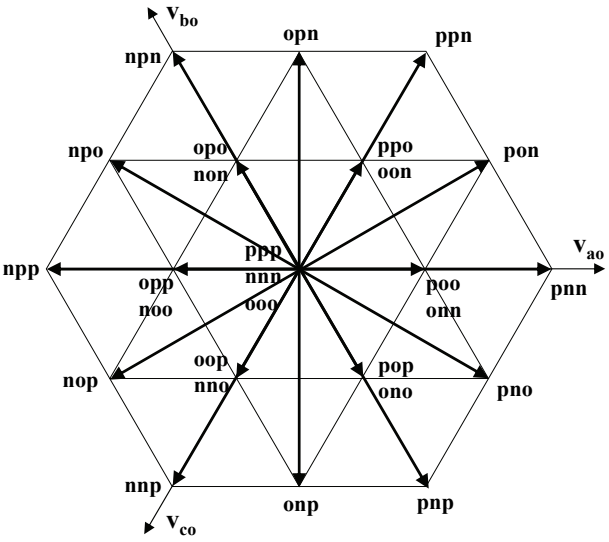

Fig. 3. Voltage vectors and switching states that can be generated by a NPC converter.

The practical implementation of FCS-MPC requires to consider the effect of the delay in the actuation due to the time needed for the measurements through analog-to-digital converters and algorithm calculations. Therefore, the discrete-time equations of the model are shifted one step forward in order to consider this time delay [37]. Applying this time shift to the discrete-time equations (8) and (9), it results

$$i(k+2)=\frac{T_s}{L}\left[v_{NPC}(k+1)-e(k+1)\right]+\left(1-\frac{R\cdot T_s}{L}\right)i(k+1) \quad (12)$$

$$\begin{aligned} v_p(k+2)&=v_p(k+1)+\frac{T_s}{C}i_{Cp}(k+1)\\ v_n(k+2)&=v_n(k+1)+\frac{T_s}{C}i_{Cn}(k+1)\end{aligned} \quad (13)$$

where line current vector $i(k+1)$ and dc-link capacitor voltage values $v_p(k+1)$, $v_n(k+1)$ can be estimated from (8) and (9) with the present measured line currents $i(k)$, grid voltages $e(k)$, dc-link capacitor voltages $v_p(k)$, $v_n(k)$ and the present voltage vector applied by the NPC converter $v_{NPC}(k)$. The voltage vector $v_{NPC}(k+1)$ is the actuation to be evaluated and $i_{Cp}(k+1)$ and $i_{Cn}(k+1)$ are obtained from the evaluated switching state and the estimated line currents.

The future value of the grid voltage vector $e(k+1)$ can be obtained from the second degree Lagrange interpolation

$$e(k+1)=3\cdot e(k)-3\cdot e(k-1)+e(k-2) \quad (14)$$

For a small enough sampling time and to save computational efforts, it is possible to consider e(k+1) ≈ e(k).

III. Control Description.

Among the different possible MPC techniques applied to power converters, the FCS-MPC is particularly interesting for multilevel topologies, as the system used in this work, since this control applies the optimized switching state directly to the converter, without using complex modulation techniques such as multilevel PWM or Space Vector Modulation (SVM).

The proposed control system has three main control objectives: delivering symmetrical and balanced ac currents to the grid, keeping balanced the dc-link capacitor voltages, and fulfilling the LVRT requirements. As detailed in this section, these control objectives are accomplished by minimizing a given quality function, which considers the tracking of a current reference and the dc-link capacitor voltage unbalance.

Some other control objectives such as the reduction of the number of commutations [19], [23] or an imposed load current spectrum [24], which are interesting for high power systems, like the system in Fig. 1, have not been considered in this work for simplicity. However, they can be included in the quality function of the predictive controller.

A. Predictive control algorithm description.

The control block diagram is shown in Fig. 2. The future value of the line current $i(k+2)$ and dc-link capacitor voltage values $v_p(k+2)$, $v_n(k+2)$ are predicted for the 27 switching states generated by the NPC inverter, by using (12) and (13). In order to do these predictions, it is necessary to measure the present value of the line currents $i(k)$, grid voltages $e(k)$ and dc-link capacitor voltages $v_p(k)$, $v_n(k)$. The estimated values at the instant $k+1$, needed for the predictions at the instant $k+2$, are calculated, by using (8) and (9), with these measurements and the present switching state applied to the NPC inverter. Once these predicted values are calculated, a quality function g is evaluated for all the switching states. The switching state which minimizes the quality function g is selected to be applied to the NPC inverter at the beginning of the next sampling period. The flow diagram for the proposed predictive algorithm is shown in Fig. 4, and the proposed quality function g is

$$g=f\left(i^*(k+2),i(k+2)\right)+\lambda_{DC}\cdot h\left(v_p(k+2),v_n(k+2)\right). \quad (15)$$

The first term in (15), $f(i^*(k+2), i(k+2))$, is dedicated to achieve the reference tracking, quantifying the difference between the current reference $i^*(k+2)$ and the predicted current for a given switching state $i(k+2)$. The proposed composition of this term is shown in (16).

$$\begin{aligned} f\left(i^*(k+2),i(k+2)\right)=&\left(i_\alpha^*(k+2)-i_\alpha(k+2)\right)^2+\\ &+\left(i_\beta^*(k+2)-i_\beta(k+2)\right)^2\end{aligned} \quad (16)$$

The second term in (15), $h(v_p(k+2), v_n(k+2))$, takes advantage of the redundant switching states of the NPC converter to balance the dc-link capacitor voltages, since the term f only considers the voltage vector. The proposed composition for this term is shown in (17). For a voltage vector with redundant switching states, the switching state which produces a smaller value for this term will be selected.

$$h\left(v_p(k+2),v_n(k+2)\right)=\left(v_p(k+2)-v_n(k+2)\right)^2 \quad (17)$$

The weighting factor λ_{DC} handles the relation between the terms dedicated to the reference tracking f, and the voltage

balance h. Some guidelines for weighting factor design are found in [15]. In this work, $\lambda_{DC} = 1$.

An estimation of the current reference for the instant $k+2$, i.e., $i^*(k+2)$, is needed for the predictive control strategy, as can be observed in (16). Depending on the length of the applied sampling period T_s, and the computational constraints, this estimation can be obtained through a second order extrapolation

$$i^*(k+2) = 6 \cdot i^*(k) - 8 \cdot i^*(k-1) + 3 \cdot i^*(k-2) \qquad (18)$$

For a small enough sampling period and also to save computational efforts it is possible to consider $i^*(k+2) \approx i^*(k)$, thus no extrapolation is needed.

Finally, notice that the analysis of the stability and bounds for the controller and system presented here is beyond the scope of this work. However, the study of the stability and bounds of the FCS-MPC applied to power converters can be found in [38], [39].

B. *Control to meet the LVRT requirements.*

In normal operation, the NPC inverter delivers to the grid the active power (active current) and delivers/absorbs the reactive power (reactive current) set by the power system operator, accordingly to the quasi-stationary operation requirements specified in the GCRs.

The LVRT requirements, extracted from the GCR of the utility operator E-ON [3], are shown in Figs. 5 and 6. When a grid voltage sag appears, the power generation plant must remain connected to the grid if the line voltage remains over the limit line in Fig. 5. In parallel, the WECS has to deliver into the grid the amount of reactive current specified in Fig. 6 to give support to the network to hold the grid voltage. The amount of reactive power to be injected depends on the percentage of grid voltage reduction during the dip, the system rated current, and the reactive current given to the grid before the dip appearance. However, little information is given about the active current. Energinet [4] specifies that "active power must be maintained during voltage drops, but a reduction in active power within the wind power plant's design specifications is acceptable, however". Moreover, in case of single- or two-phase voltage dips, there are few specifications in the GCRs, so there may be certain ambiguity regarding which should be the control strategy to meet the LVRT requirements. In any case, this control must take place within a time limit after fault recognition, for instance 20 ms (E-ON) [3].

After fault clearance, some GCRs demand to maintain the voltage support by injecting reactive current for a time, for instance 500 ms (E-ON) [3], and an active power recover to the original value with a minimum gradient, for instance 20% of the rated power per second (E-ON) [3].

A voltage sag detection and identification is needed, as shown in Fig. 2, to provide the proper control action as function of any specific voltage sag type and depth, accordingly with the LVRT requirements. Some methods are reported [40], [41], which provide detection within 1 ms [42]–[44] after the perturbation appearance. In this work, for the sake of simplicity, this detection has not been implemented, because the voltage dip type and depth is previously known, as it is set by the user both at our experimental setup and the simulations.

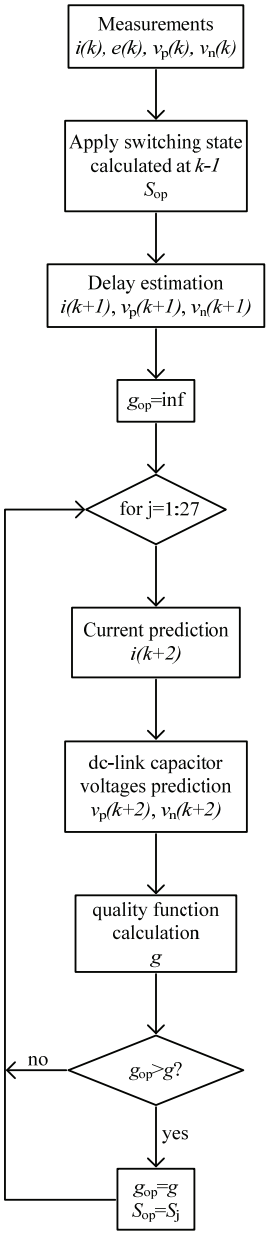

Fig. 4. Predictive control algorithm flow diagram.

There are different strategies to generate the current reference to meet the LVRT requirement, as discussed in [16], [45]. In this work, the generated *abc* current references are symmetrical and balanced at all time, as in the Vector Current Controller with Feedforward of negative sequence voltage (VCCF) strategy [45]. To do that, the current reference requires to be synchronized with the grid voltage. The Phase-Locked-Loop (PLL) detailed in [34] has been used to obtain the voltage grid angle θ_g, as shown in Fig. 2, guaranteeing angle precision both in normal operation and under balanced/unbalanced grid fault condition. Therefore, the

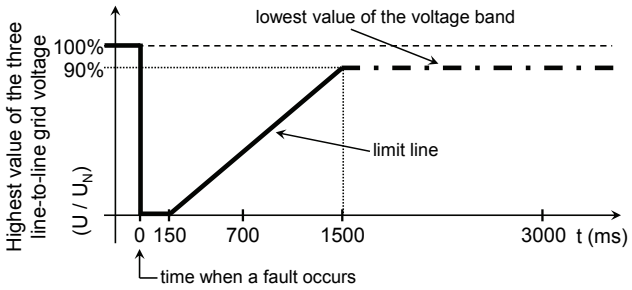

Fig. 5. Voltage limit curve to allow generator disconnection.

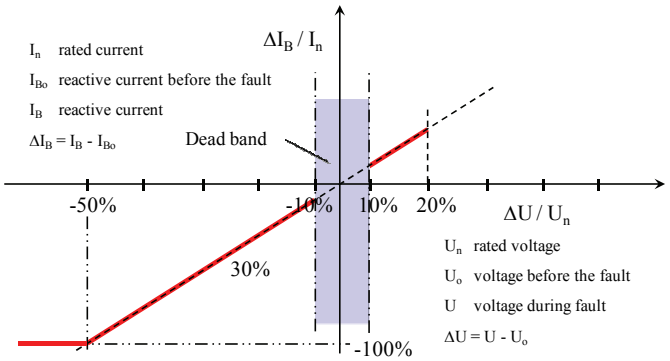

Fig. 6. Reactive current to be delivered to the grid under a voltage dip.

symmetrical and balanced *abc* current references are generated (19) with the current amplitude (I^*) and phase angle (φ^*) with respect the grid voltage, obtained from the active (I_A^*) and reactive (I_R^*) current references, by using (20). The current amplitude is limited to the maximum available current that the converter can supply.

$$\begin{aligned} i_a^*(t) &= I^* \cos\left(\theta_g + \varphi^*\right) \\ i_b^*(t) &= I^* \cos\left(\theta_g - 2\pi/3 + \varphi^*\right) \\ i_c^*(t) &= I^* \cos\left(\theta_g + 2\pi/3 + \varphi^*\right) \end{aligned} \tag{19}$$

$$I^* = \sqrt{\left(I_A^*\right)^2 + \left(I_R^*\right)^2} \quad ; \quad \varphi^* = arctg\frac{I_R^*}{I_A^*} \tag{20}$$

The active (I_A^*) and reactive (I_R^*) current references are set by the power system operator in steady-state, and by the LVRT requirements as function of the grid voltage depth and type. With this approach, the proposed controller can be adapted to meet any GCRs by appropriate adjustment of the reference. Notice that, with the predictive control applied here, the symmetrical components are not used for control purposes and therefore, a SSM is not needed.

IV. Simulation Results

Simulation results (MatLab-Simulink) for the proposed predictive controller are presented in this section. The specifications for the system in Fig. 2, obtained from the experimental setup described in the next section, are: V_{pn} = 300 V ; C = 2.2 mF ; L = 5.5 mH ; R = 0.5 Ω ; V_{grid} = 152 V_{RMS} ; f_{grid} = 50 Hz ; and sampling period T_s = 100 µs.

The current reference values for steady-state operation are I^* = 4 A and φ^* = 0 rad, thus working at unity power factor. During the voltage dip their values are shifted in order to fulfill the LVRT.

Two different grid voltage dips, type B and type C [46], have been simulated in order to show the controller performance and compare them with the experimental results shown in the next section.

A. Simulation results for a grid dip type B.

The simulated grid phase voltages are shown in Fig. 7(a). At t = 50 ms, the voltage for the phase *a* drops to 11% of its nominal value during 60 ms, with a phase shift of π/6 rad (lagging) to simulate the real behavior of the grid in the experimental setup, as shown in Section V. According to the LVRT requirements [3], the inverter must deliver all its rated current as reactive current to the grid (Fig. 6), so the current reference values change to I^* = 6 A and φ^* = π/2 rad. Balanced grid currents are delivered to the grid at all times, see Fig. 7(b) and Fig. 7(c), which show a fast and accurate transient performance with no overshoot. The dc-link capacitor voltages are kept balanced at all times, as shown in Fig. 7(d). Instant and average active and reactive power are shown in Fig. 7(e). In steady-state operation the system works at unity power factor, the average active power delivered to the grid is around 900 W and the average reactive power is 0 VAR. Under grid dip condition, the average active power delivered to the grid is 0 W and the average reactive power is around 960 VAR, fulfilling the LVRT requirements. Instant active and reactive power oscillate at 2ω because balanced line currents and unbalanced grid voltages are present.

B. Simulation results for a grid dip type C.

The simulated grid phase voltages are shown in Fig. 8(a). At t = 50 ms phase *a* and phase *b* voltages drops to 62.5% of their nominal value with a phase shift of π/7 rad during 60 ms. In order to fulfill the LVRT requirements the inverter must deliver a minimum of 75% of its rated current as reactive current the remaining rated current is delivered as active current as specified in Fig. 6, so the current references change to I^* = 6 A and φ^* = 0.848 rad. Similar results as for the grid dip type B are shown here: balanced grid currents at all times, Fig. 8(b), with fast transient performance with no overshoot, Fig. 8(c), and balanced dc-link capacitor voltages, Fig.8(d). The active and reactive power, Fig. 8(e), differ from the dip B case as active and reactive current are delivered to the grid, instead of delivering only reactive current. The average values on steady state are the same as in the last subsection, while under grid dip the average active power is around 600 W and the average reactive power is around 700 VAR.

C. Current tracking and reduction of commutations.

As it can be observed in Fig. 9, FCS-MPC presents good dynamic response and reference tracking.

The accumulated number of commutations for all the switches in phase *a*, switches S_{a4}, S_{a3}, S_{a2}, and S_{a1} in Fig. 2, in steady-state operation for a line period, is compared in Fig. 10 between a SVM technique (f_s = 5 kHz) [47], used in [29] and the proposed FCS-MPC. The sampling period used here for the FCS-MPC (T_s = 100 µs), gives a maximum switching

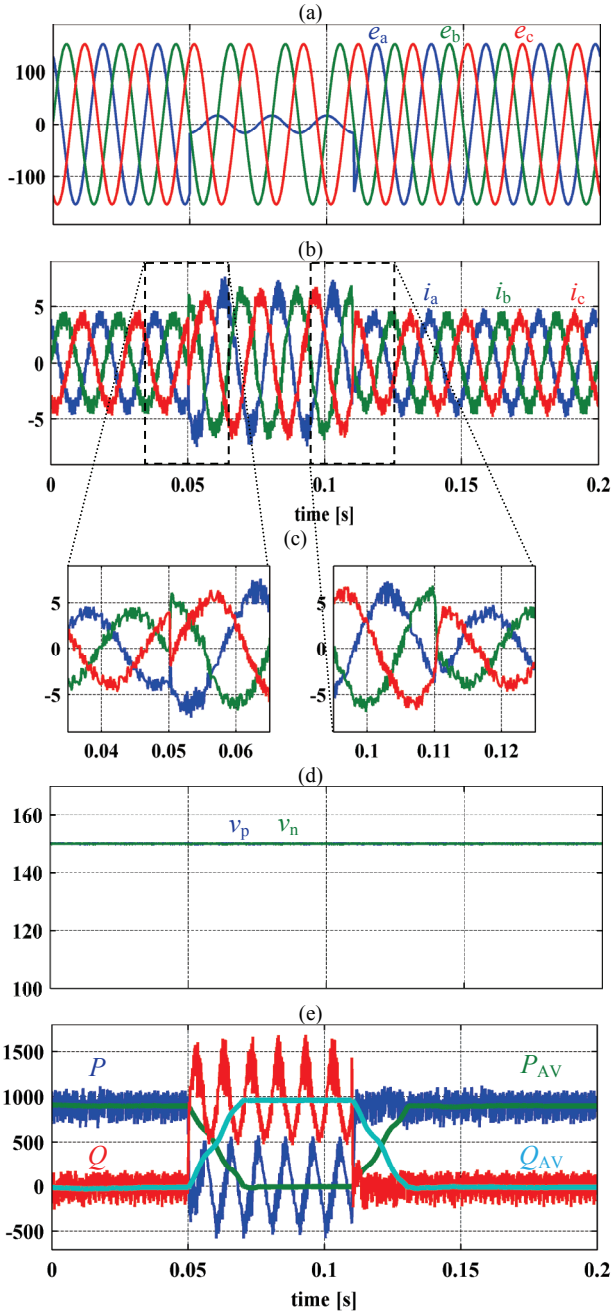

Fig. 7. Simulation of the dynamic response during a grid voltage dip type B. (a) Grid voltages e_a , e_b , e_c (V). (b) Line currents i_a , i_b , i_c (A). (c) Detail of the transient behavior of the line currents i_a , i_b , i_c (A). (d) Dc-link capacitor voltages v_p , v_n (V). (e) Instant P , Q and average P_{AV} , Q_{AV} active and reactive power delivered to the grid (W,VAR).

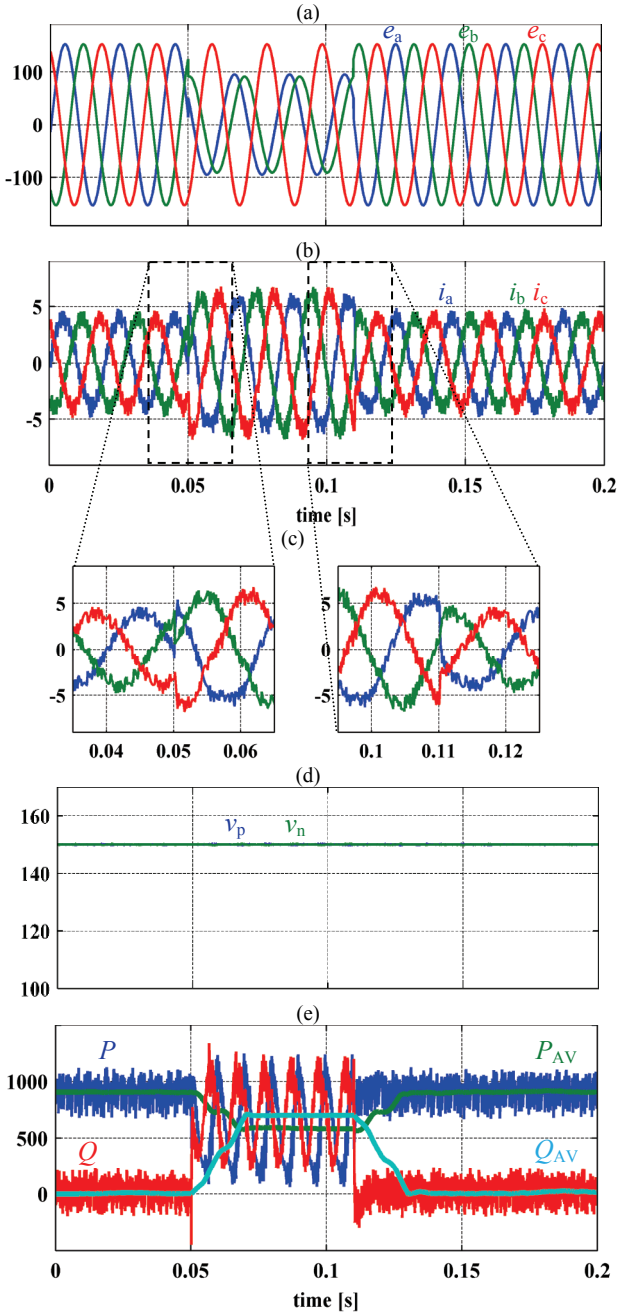

Fig. 8. Simulation of the dynamic response during a grid voltage dip type C. (a) Grid voltages e_a , e_b , e_c (V). (b) Line currents i_a , i_b , i_c (A). (c) Detail of the transient behavior of the line currents i_a , i_b , i_c (A). (d) Dc-link capacitor voltages v_p , v_n (V). (e) Instant P , Q and average P_{AV} , Q_{AV} active and reactive power delivered to the grid (W,VAR).

frequency of 5 kHz. Results in Fig. 10 show that, with the proposed FCS-MPC, the number of commutations is reduced about 85% compared to this specific SVM [47]. Thus, the accumulated number of commutations for all the converter switches using the proposed FCS-MPC are lower than the accumulated number of commutations for only one branch with this specific SVM. Although the analysis of the converter losses with the proposed predictive control is beyond the scope of this work, the reduction of the number of commutations produces lower losses.

Notice that the number of commutations can be even more reduced by including an additional term in the quality function [19], [23], also providing some degree of decoupling between the sampling and the switching frequencies. Hence the predictive control algorithm will run with high sampling frequency but low switching frequency.

As the FCS-MPC selects the best voltage vector that minimizes the quality function, there are time intervals where the voltage vector does not change so the converter does not commutate. Also, there are some time intervals where a given branch remains connected to the same dc-voltage level while

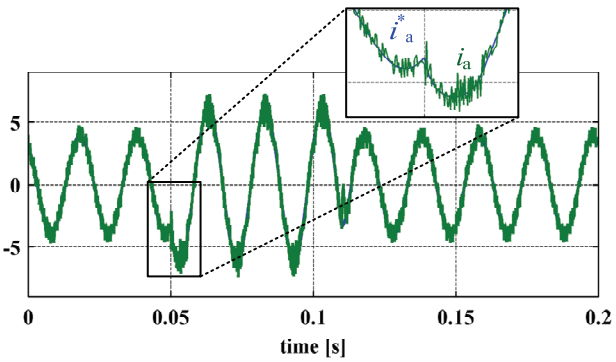

Fig. 9. Simulation of the dynamic response and reference tracking for the line current i_a (A) when a voltage dip B is present.

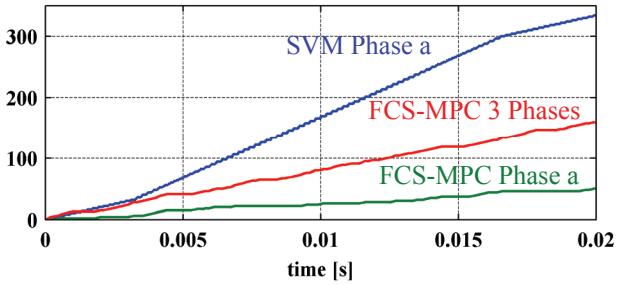

Fig. 10. Comparison of the simulated accumulated number of commutations for all the switches in phase a (S_{a4}, S_{a3}, S_{a2}, and S_{a1}) in Fig. 2 for a line period, with a SVM [47] and with FCS-MPC.

the other branches commutate, so the accumulated commutations for a single branch do not increase while the accumulated commutations for the whole converter increase, as it can be observed in Fig. 10.

The phase a load current spectrum and THD is compared for the SVM [47], Fig. 11, and for the FCS-MPC, Fig. 12. Higher THD is found for the FCS-MPC, as previously detailed in [19]. With FCS-MPC, grid currents present some low frequency harmonics, as shown in Fig. 12, that could excite some resonances in the grid. However, the FCS-MPC can achieve better performance than the SVM by using a proper weight in the quality function for controlling the switching frequency [19] or the current spectrum [24]. Regarding to the filter performance, the FCS-MPC operation with variable switching frequency can make more difficult the design of any filter or deteriorate its performance. For this reason, strategies of predictive control working with constant switching frequency are under development.

V. Experimental Results

This section presents the experimental results obtained for the proposed control strategy depicted in Fig. 2. The experimental setup is a part of a wind emulation platform shown in Fig. 13.

The experimental results are obtained using one of the two NPC converters included in the back-to-back cabinet. The specifications for the system have been detailed in the previous section.

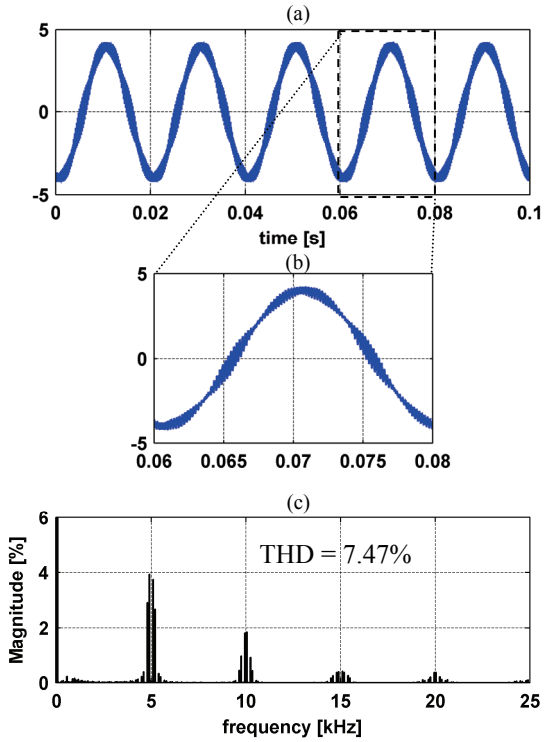

Fig. 11. Simulation of the phase *a* load current for a SVM [47]. (a) Time domain waveform for 5 grid cycles. (b) Time domain waveform for the FFT and THD analysis (1 grid cycle). (c) Harmonic spectrum for 1 grid cycle.

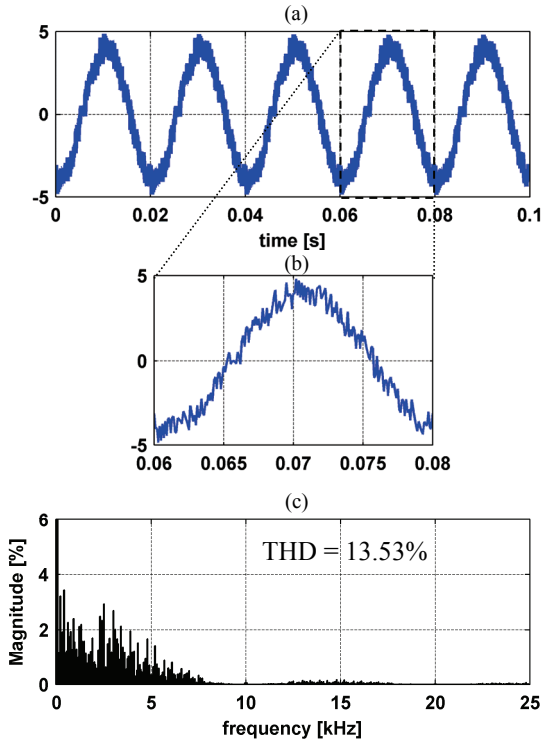

Fig. 12. Simulation of the phase *a* load current for the FCS-MPC. (a) Time domain waveform for 5 grid cycles. (b) Time domain waveform for the FFT and THD analysis (1 grid cycle). (c) Harmonic spectrum for 1 grid cycle.

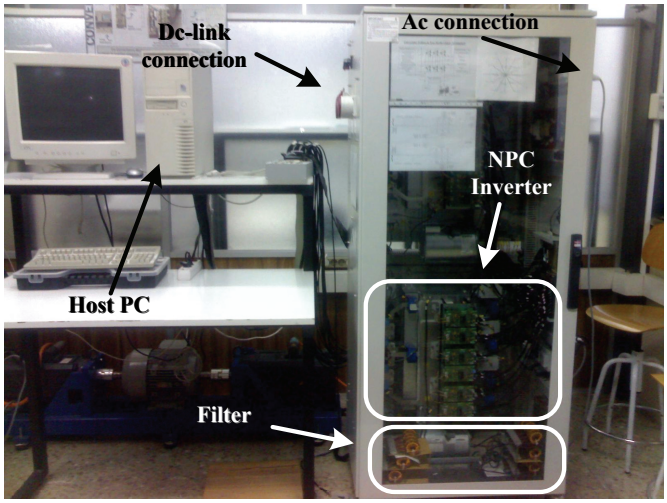

Fig. 13. Experimental setup overview.

Dips have been generated at the laboratory by switching one grid phase from its rated voltage to a smaller voltage generated by a single-phase autotransformer, using two bidirectional electronic switches.

Notice that good agreement has been found between simulations and experimental results in all cases.

A. Experimental results for a grid dip type B.

Fig. 14(a) shows grid phase voltages, where phase *a* suffers a 89% voltage drop during 60 ms (starting at t = 50 ms) with a $\pi/6$ rad (lagging) phase shift. Line currents shown in Fig. 14(b) are balanced before and after the grid dip and present a good balance during the grid disturbance with a fast and accurate transient performance with no overshoot, Fig. 14(c). Dc-link capacitor voltages are balanced at all times, as shown in Fig. 14(d).

Under dip condition, in order to meet the LVRT requirements shown in Figs. 5 and 6, the current reference is changed to I^* = 6 A and $\varphi^* = \pi/2$ rad, the average active power delivered to the grid is 0 W and the average reactive power delivered to the grid is about 990 VAR, while in steady-state operation the average active power delivered to the grid is around 910 W and the average reactive power delivered to the grid is around 0 VAR.

B. Experimental results for a grid dip type C.

Grid phase voltages, where phase *a* and phase *b* suffer a 32.5% voltage drop and a phase shift of $\pi/7$ rad during 60 ms (starting at t = 50 ms), are shown in Fig. 15(a). Line currents are balanced at all times and present good transient response and reference tracking, see Fig. 15(b) and Fig. 15(c). Dc-link capacitor voltages, Fig. 15(d), are kept balanced.

In steady-state operation, the system works at unity power factor, and therefore the average active power delivered to the grid is around 910 W and the average reactive power delivered to the grid is around 0 VAR, as shown in Fig. 15(e). Under dip condition, the LVRT requirements demand to inject a reactive

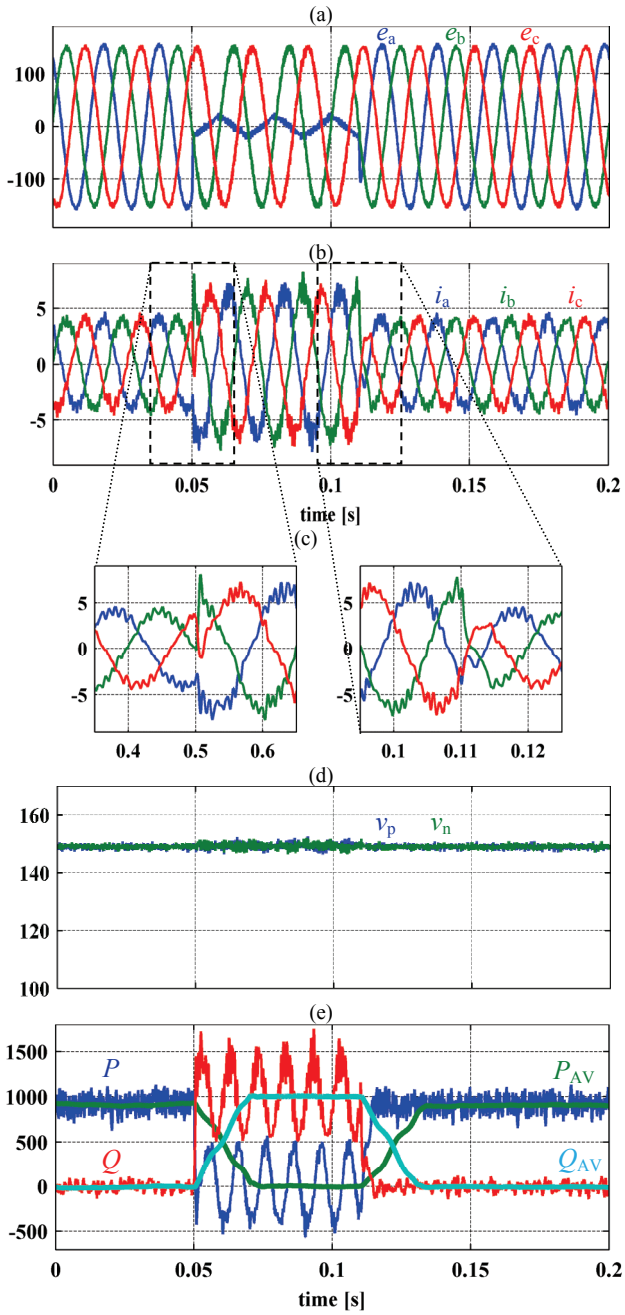

Fig. 14. Experimental results of the dynamic response during a grid voltage dip type B. All variables obtained from the dSPACE readings. (a) Grid voltages e_a , e_b , e_c (V). (b) Line currents i_a , i_b , i_c (A). (c) Detail of the transient behavior of the line currents i_a , i_b , i_c (A). (d) Dc-link capacitor voltages v_p , v_n (V). (e) Instant P , Q and average P_{AV} , Q_{AV} active and reactive power delivered to the grid (W,VAR).

current of 75% of the system rated current. The current reference is properly changed and, under grid disturbance condition, the average active power delivered to the grid is about 650 W and the average reactive power delivered to the grid is about 750 VAR. Notice the oscillations in the instant active and reactive power, as detailed in the previous section.

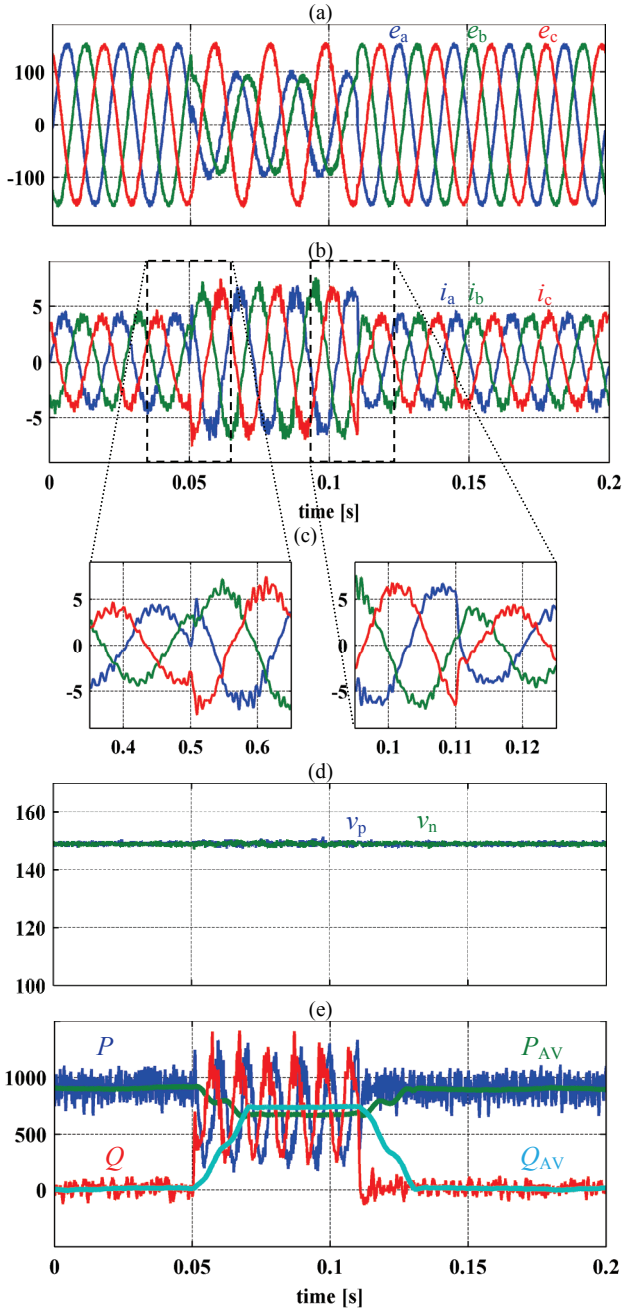

Fig. 15. Experimental results of the dynamic response during a grid voltage dip type C. All variables obtained from the dSPACE readings. (a) Grid voltages e_a , e_b , e_c (V). (b) Line currents i_a , i_b , i_c (A). (c) Detail of the transient behavior of the line currents i_a , i_b , i_c (A). (d) Dc-link capacitor voltages v_p , v_n (V). (e) Instant P , Q and average P_{AV} , Q_{AV} active and reactive power delivered to the grid (W,VAR).

VI. Conclusion

A finite control set model predictive current controller has been proposed for the grid-side NPC converter of a wind energy conversion system in order to meet the LVRT requirements. Simulations and experimental results strongly agree and show good system performance.

The proposed controller can be adapted to meet any GCRs, and provides balanced line currents at all time. The current reference tracking performance is fast, accurate and presents

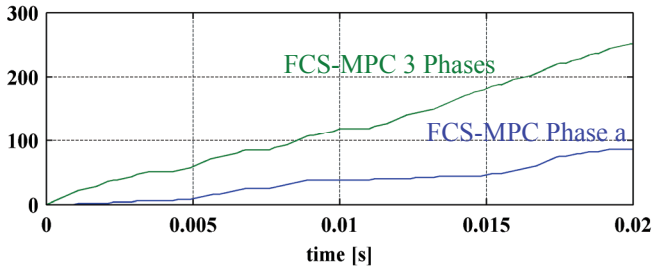

Fig. 16. Accumulated number of commutations for the experimental setup with FCS-MPC.

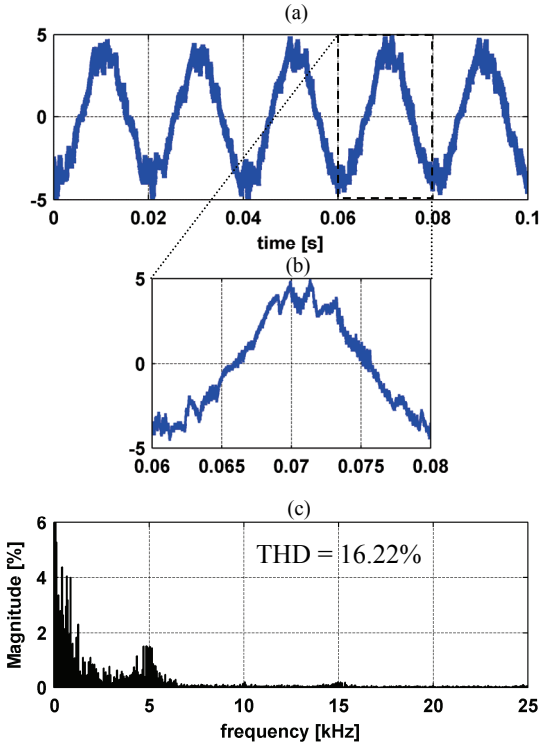

Fig. 17. Phase *a* load current for the experimental setup with FCS-MPC. (a) Time domain waveform for 5 grid cycles. (b) Time domain waveform for the FFT and THD analysis (1 grid cycle). (c) Harmonic spectrum for 1 grid cycle.

no overshoot, furthermore with a smaller number of commutations in comparison with PWM, reducing the switching losses. This performance can be even enhanced by adding an additional term in the quality function to reduce commutations and improve the current spectrum.

In parallel, the predictive controller uses the redundant states of the three-level inverter to keep balanced the dc-link capacitor voltages at all time.

Finally, the predictive control method proposed in this paper is much simpler than the classical solutions.

References

[1] European Comission. (EurObserv'ER), "Wind Energy Barometer 2012," *Systèmes Solaires - Le J. l'Éolien*, no. 12, pp. 46–69, 2013.

[2] M. Altın, O. Göksu, R. Teodorescu, P. Rodriguez, B.-B. Jensen, and L. Helle, "Overview of recent grid codes for wind power integration," *IEEE Int. Conf. Optim. Electr. Electron. Equip.*, pp. 1152–1160, 2010.

[3] E. ON Netz GmbH, "Grid Code: High and extra high voltage," 2006. [Online]. Available: www.eon-netz.com. [Accessed: 05-Nov-2013].
[4] Energinet, "Technical regulation 3.2.5 for wind power plants with a power output greater than 11 kW," 2010. [Online]. Available: www.energinet.dk. [Accessed: 05-Nov-2013].
[5] M. Liserre, R. Cardenas, M. Molinas, and J. Rodriguez, "Overview of Multi-MW Wind Turbines and Wind Parks," *IEEE Trans. Ind. Electron.*, vol. 58, no. 4, pp. 1081–1095, Apr. 2011.
[6] R. Cardenas, R. Pena, S. Alepuz, and G. Asher, "Overview of Control Systems for the Operation of DFIGs in Wind Energy Applications," *IEEE Trans. Ind. Electron.*, vol. 60, pp. 1–1, 2013.
[7] B. Wu, Y. Lang, N. Zargari, and S. Kouro, *Power Conversion and Control of Wind Energy Systems*. Wiley-IEEE Press, 2011.
[8] Z. Chen, J. M. Guerrero, and F. Blaabjerg, "A Review of the State of the Art of Power Electronics for Wind Turbines," *IEEE Trans. Power Electron.*, vol. 24, no. 8, pp. 1859–1875, Aug. 2009.
[9] M. Popat, B. Wu, and N. R. Zargari, "Fault Ride-Through Capability of Cascaded Current-Source Converter-Based Offshore Wind Farm," *IEEE Trans. Sustain. Energy*, vol. 4, no. 2, pp. 314–323, Apr. 2013.
[10] S. Kouro, M. Malinowski, K. Gopakumar, J. Pou, L. G. Franquelo, B. Wu, J. Rodriguez, M. A. Pérez, and J. I. Leon, "Recent Advances and Industrial Applications of Multilevel Converters," *IEEE Trans. Ind. Electron.*, vol. 57, no. 8, pp. 2553–2580, Aug. 2010.
[11] J. Rodriguez, S. Bernet, P. K. Steimer, and I. E. Lizama, "A Survey on Neutral-Point-Clamped Inverters," *IEEE Trans. Ind. Electron.*, vol. 57, no. 7, pp. 2219–2230, Jul. 2010.
[12] E. F. Camacho and C. Bordons Alba, *Model Predictive Control*, 2nd ed. Springer, 2004, p. 405.
[13] J. Rodriguez, M. P. Kazmierkowski, J. R. Espinoza, P. Zanchetta, H. Abu-Rub, H. A. Young, and C. A. Rojas, "State of the Art of Finite Control Set Model Predictive Control in Power Electronics," *IEEE Trans. Ind. Informatics*, vol. 9, no. 2, pp. 1003–1016, May 2013.
[14] A. Linder, R. Kanchan, R. Kennel, and P. Stolze, *Model-Based Predictive Control of Electric Drives*. Cuvillier Verlag Göttingen, 2010.
[15] J. Rodriguez and P. Cortes, *Predictive Control of Power Converters and Electrical Drives*. Wiley-IEEE Press, 2012.
[16] S. Alepuz, S. Busquets-Monge, J. Bordonau, P. Cortes, and S. Kouro, "Control methods for Low Voltage Ride-Through compliance in grid-connected NPC converter based wind power systems using predictive control," in *IEEE Energy Conversion Congress and Exposition (ECCE)*, 2009, pp. 363–369.
[17] J. D. Barros and J. F. Silva, "Optimal Predictive Control of Three-Phase NPC Multilevel Inverter: Comparison to Robust Sliding Mode Controller," in *IEEE Power Electronics Specialists Conference (PESC)*, 2007, pp. 2061–2067.
[18] J. D. Barros, J. F. A. Silva, and É. G. A. Jesus, "Fast-Predictive Optimal Control of NPC Multilevel Converters," *IEEE Trans. Ind. Electron.*, vol. 60, no. 2, pp. 619–627, Feb. 2013.
[19] P. Cortes, L. Vattuone, and J. Rodriguez, "A comparative study of predictive current control for three-phase voltage source inverters based on switching frequency and current error," in *European Conference on Power Electronics and Applications (EPE)*, 2011, pp. 1–8.
[20] P. Cortes, M. P. Kazmierkowski, R. M. Kennel, D. E. Quevedo, and J. Rodriguez, "Predictive Control in Power Electronics and Drives," *IEEE Trans. Ind. Electron.*, vol. 55, no. 12, pp. 4312–4324, Dec. 2008.
[21] S. Muller, U. Ammann, and S. Rees, "New Time-Discrete Modulation Scheme for Matrix Converters," *IEEE Trans. Ind. Electron.*, vol. 52, no. 6, pp. 1607–1615, Dec. 2005.
[22] S. Kouro, P. Cortes, R. Vargas, U. Ammann, and J. Rodriguez, "Model Predictive Control—A Simple and Powerful Method to Control Power Converters," *IEEE Trans. Ind. Electron.*, vol. 56, no. 6, pp. 1826–1838, Jun. 2009.
[23] R. Vargas, P. Cortes, U. Ammann, J. Rodriguez, and J. Pontt, "Predictive Control of a Three-Phase Neutral-Point-Clamped Inverter," *IEEE Trans. Ind. Electron.*, vol. 54, no. 5, pp. 2697–2705, Oct. 2007.
[24] P. Cortes, J. Rodriguez, D. E. Quevedo, and C. Silva, "Predictive Current Control Strategy With Imposed Load Current Spectrum," *IEEE Trans. Power Electron.*, vol. 23, no. 2, pp. 612–618, Mar. 2008.
[25] C.-T. Lee, C.-W. Hsu, and P.-T. Cheng, "A Low-Voltage Ride-Through Technique for Grid-Connected Converters of Distributed Energy Resources," *IEEE Trans. Ind. Appl.*, vol. 47, no. 4, pp. 1821–1832, Jul. 2011.
[26] K.-H. Kim, Y.-C. Jeung, D.-C. Lee, and H.-G. Kim, "LVRT Scheme of PMSG Wind Power Systems Based on Feedback Linearization," *IEEE Trans. Power Electron.*, vol. 27, no. 5, pp. 2376–2384, May 2012.
[27] M. Fatu, C. Lascu, G.-D. Andreescu, R. Teodorescu, F. Blaabjerg, and I. Boldea, "Voltage Sags Ride-Through of Motion Sensorless Controlled PMSG for Wind Turbines," in *IEEE Industry Applications Annual Meeting (IAS)*, 2007, pp. 171–178.
[28] S. M. Muyeen, R. Takahashi, T. Murata, and J. Tamura, "A Variable Speed Wind Turbine Control Strategy to Meet Wind Farm Grid Code Requirements," *IEEE Trans. Power Syst.*, vol. 25, no. 1, pp. 331–340, Feb. 2010.
[29] S. Alepuz, A. Calle, S. Busquets-Monge, S. Kouro, and B. Wu, "Use of Stored Energy in PMSG Rotor Inertia for Low-Voltage Ride-Through in Back-to-Back NPC Converter-Based Wind Power Systems," *IEEE Trans. Ind. Electron.*, vol. 60, no. 5, pp. 1787–1796, May 2013.
[30] J. Hu, Y. He, L. Xu, and D. Zhi, "Predictive current control of grid-connected voltage source converters during network unbalance," *IET Power Electron.*, vol. 3, no. 5, p. 690, 2010.
[31] Z. He, D. Sun, L. Shang, and J. G. Zhu, "Modified predictive direct power control of voltage-sourced converters under network voltage unbalance conditions," in *IEEE International Conference on Electrical Machines and Systems (ICEMS)*, 2011, pp. 1–6.
[32] G. Hou, Z. Wang, P. Jiang, and J. Zhang, "Multivariable predictive functional control applied to doubly fed induction generator under unbalanced grid voltage conditions," in *IEEE Conference on Industrial Electronics and Applications (ICIEA)*, 2009, pp. 2644–2650.
[33] S. Alepuz, S. Busquets-Monge, J. Bordonau, P. Cortes, J. Rodriguez, and R. Vargas, "Predictive current control of grid-connected neutral-point-clamped converters to meet low voltage ride-through requirements," in *IEEE Power Electronics Specialists Conference (PESC)*, 2008, pp. 2423–2428.
[34] S. Alepuz, S. Busquets-Monge, J. Bordonau, J. A. Martinez-Velasco, C. A. Silva, J. Pontt, and J. Rodriguez, "Control Strategies Based on Symmetrical Components for Grid-Connected Converters Under Voltage Dips," *IEEE Trans. Ind. Electron.*, vol. 56, no. 6, pp. 2162–2173, Jun. 2009.
[35] K. Ma, F. Blaabjerg, and M. Liserre, "Thermal Analysis of Multilevel Grid-Side Converters for 10-MW Wind Turbines Under Low-Voltage Ride Through," *IEEE Trans. Ind. Appl.*, vol. 49, no. 2, pp. 909–921, Mar. 2013.
[36] J. F. Conroy and R. Watson, "Low-voltage ride-through of a full converter wind turbine with permanent magnet generator," *IET Renew. Power Gener.*, vol. 1, no. 3, p. 182, 2007.
[37] P. Cortes, J. Rodriguez, C. Silva, and A. Flores, "Delay Compensation in Model Predictive Current Control of a Three-Phase Inverter," *IEEE Trans. Ind. Electron.*, vol. 59, no. 2, pp. 1323–1325, Feb. 2012.
[38] R. P. Aguilera and D. E. Quevedo, "On stability and performance of finite control set MPC for power converters," in *Workshop on Predictive Control of Electrical Drives and Power Electronics (PRECEDE)*, 2011, pp. 55–62.
[39] T. Geyer, R. P. Aguilera, and D. E. Quevedo, "On the stability and robustness of model predictive direct current control," in *IEEE International Conference on Industrial Technology (ICIT)*, 2013, pp. 374–379.
[40] M. Mansor and N. A. Rahim, "Voltage sag detection - A survey," in *International Conference for Technical Postgraduates (TECHPOS)*, 2009, pp. 1–6.
[41] P. Thakur, A. K. Singh, and R. C. Bansal, "Novel way for classification and type detection of voltage sag," *IET Gener. Transm. Distrib.*, vol. 7, no. 4, pp. 398–404, Apr. 2013.
[42] B. Bae, J. Jeong, J. Lee, and B. Han, "Novel Sag Detection Method for Line-Interactive Dynamic Voltage Restorer," *IEEE Trans. Power Deliv.*, vol. 25, no. 2, pp. 1210–1211, Apr. 2010.
[43] Y. Kumsuwan and Y. Sillapawicharn, "A fast synchronously rotating reference frame-based voltage sag detection under practical

grid voltages for voltage sag compensation systems," in *International Conference on Power Electronics, Machines and Drives (PEMD)*, 2012, pp. 1–5.

[44] A. K. Sadigh and K. M. Smedley, "Fast voltage sag detection method for single-/three-phase application," in *IEEE Applied Power Electronics Conference and Exposition (APEC)*, 2013, pp. 881–888.

[45] G. Saccomando, J. Svensson, and A. Sannino, "Improving voltage disturbance rejection for variable-speed wind turbines," *IEEE Trans. Energy Convers.*, vol. 17, no. 3, pp. 422–428, Sep. 2002.

[46] M. Bollen, *Understanding power quality problems: voltage sags and interruptions*. IEEE Press, 1999.

[47] S. Busquets-Monge, J. Bordonau, D.Boroyevich, and S. Somavilla, "The nearest three virtual space vector PWM - a modulation for the comprehensive neutral-point balancing in the three-level NPC inverter," *IEEE Power Electron. Lett.*, vol. 2, no. 1, pp. 11-15, Mar. 2004.

Alejandro Calle-Prado (S'11) was born in Barcelona, Spain. He received the B. Sc. and M. Sc. degrees in electrical engineering from the Technical University of Catalonia (UPC), Barcelona, Spain, in 2008, where he is currently working toward the Ph. D. degree in electrical engineering.

Since 2008, he has been a Researcher in the Power Electronics Research Centre, UPC. His research interests include multilevel power converters applied to renewable energy systems.

Salvador Alepuz (S'98-M'03-SM'12) was born in Barcelona, Spain. He received the M.Sc. and Ph.D degrees in electrical and electronic engineering from the Technical University of Catalonia (UPC), Barcelona, Spain, in 1993 and 2004, respectively.

Since 1994, he has been Associate Professor at the Mataró School of Technology (UPC), Tecnocampus Mataró-Maresme, Mataró, (Barcelona), Spain. From 2006 to 2007, he was with the Departamento de Electrónica, Universidad Técnica Federico Santa María, Chile, developing a postdoctoral research. In 2009, he was a visiting researcher for three months at the Electrical and Computer Engineering Department, Ryerson University, Toronto, Canada. His fields of interest are multilevel conversion and ac power conversion applied to renewable energy systems.

Josep Bordonau (S'87-M'89) received the M.Sc. and the Ph.D. degrees in electrical engineering with honors from the Technical University of Catalonia, Barcelona, Spain in 1984 and 1990, respectively.

He has been a Lecturer (1984), an Assistant Professor (1990), and an Associate Professor since 1991, in the Technical University of Catalonia. Currently, he is Director of the Power Electronics Research Center of the Technical University of Catalonia and the Education Director of the Iberia Office in KIC Innoenergy. He is active in more than 30 research projects with international institutions and companies, authoring more than 70 international journal and conference papers (h index 15). His main interest is on ac converters, multilevel technology, renewable energies, energy management sytems, distributed generation systems, smart grids and electric/hybrid vehicles.

Dr. Bordonau is a member of the IEEE Technical Committee in Distributed Generation and Renewable Energy Systems.

Joan Nicolas-Apruzzese (S'11) was born in Maracaibo, Venezuela. He received the M.S. (2008) and Ph.D. (2013) in electrical engineering from the Technical University of Catalonia, Barcelona, Spain.

Since 2008, he has been a researcher in the Power Electronics Research Centre of the Technical University of Catalonia. His main research interests include power multilevel converters applied to electric vehicles and photovoltaic- and wind-energy systems.

Patricio Cortes (S'05-M'08) received the Engineer and M.Sc. degrees in electronic engineering from the Universidad Tecnica Federico Santa Maria (UTFSM), Valparaiso, Chile, in 2004. He received the Ph.D. degree at the same university in 2008. He also received the Industrial Design degree from the Pontifical Catholic University of Valparaíso in 2006.

From 2008 to 2012 he was a Research Associate at the Electronics Engineering Department, UTFSM. Since 2012 he is a postdoctoral researcher at the Power Electronic Systems Laboratory at the Swiss Federal Institute of Technology (ETH) Zurich. His main research interests are modeling and control of power converters.

Dr. Cortes received the Best Paper Award from the IEEE TRANSACTIONS ON INDUSTRIAL ELECTRONICS in 2007.

Jose Rodriguez (M'81-SM'94-F'10) received the Engineer degree in electrical engineering from the Universidad Federico Santa Maria (UTFSM), Valparaiso, Chile, in 1977 and the Dr.-Ing. degree in electrical engineering from the University of Erlangen, Erlangen, Germany, in 1985.

He has been with the Department of Electronics Engineering, University Federico Santa Maria since 1977, where he is currently full Professor and Rector. He has co-authored more than 350 journal and conference papers. His main research interests include multilevel inverters, new converter topologies, control of power converters, and adjustable-speed drives.

Prof. Rodriguez is Associate Editor of the IEEE TRANSACTIONS ON POWER ELECTRONICS, INDUSTRIAL ELECTRONICS and INDUSTRIAL INFORMATICS. He has received a number of Best Paper Awards from different IEEE Journals. Prof. Rodríguez is Fellow of the Chilean Academy of Engineering and Fellow of the IEEE. He was the recipient of the National Applied Sciences and Technology Award of Chile 2014.